Real time detection of fatigue cracks on steel structures by applying square wave induction

Paul Dario Toasa Caiza [a,*], Daiki Shiozawa [b], Thomas Ummenhofer [a], Takahide Sakagami [b]

[a] KIT Stahl- und Leichtbau, Versuchsanstalt für Stahl, Holz und Steine, Karlsruher Institut für Technologie (KIT)., Otto-Ammann-Platz 1, 76131 Karlsruhe, Germany
[b] Department of Mechanical Engineering/Graduate School of Engineering, Kobe University., 1-1, Rokkodai-cho, Nada-ku, Kobe, 657-8501, Japan

ARTICLE INFO

ABSTRACT

For years the Eddy currents principle together with inductive thermography have been applied to detect cracks or defects in metallic machine components. In case a component has a crack, by inducing Eddy currents within a coil, it is possible to cause a temperature increase in the edges of the crack. This temperature variation can be observed by using an infrared camera. Thus, the crack is registered and observed in the infrared images, which are later analyzed. However, currently used systems require an enormous amount of power and a long time for image processing. For this reason, applying this method to large steel structures such as bridges, cranes, wind power towers, pipe lines or offshore oil stations has been much more complex. To overcome these limitations, a light portable system that optimally recreates the Eddy currents principle has been developed and used in this research. This system generates a square wave AC voltage, it uses considerably less power and it is capable of detecting cracks in real time. This paper presents the simulations and experiments carried out on two different structural steel specimens to demonstrate the efficiency of the system and its potential in the field of nondestructive testing.

1. Introduction

The general principle of non-destructive testing (NDT) based on active thermography is defined as: an activation of the specimen by thermal or mechanical means in order to obtain a significant variation of the temperature field, which can reveal the presence of structural damages [1]. Particularly, the active thermography based on electromagnetic induction performs the excitation of a specimen through the generation of electromagnetic waves while an infrared (IR) camera records the variations of the surface temperature or a sensor detects changes in the Eddy current signal [2]. Thus, the magnitude and the phase images of the generated thermal fields can be observed and analyzed, so that, structural damages such as cracks or delaminations can be detected.

The physical principle can be described as follows. A high frequency sinusoidal voltage signal is generated, amplified and supplied to the coil, so that, a high frequency current signal is generated. This current flowing through the coil generates a magnetic field around the coil. And if the coil is placed close to an electrically conductive material, Eddy currents are induced in the material and flow through it. If the material contains a crack or discontinuity on the surface, the flow of the Eddy currents is disturbed, so that, they flow around the edges of the discontinuity and therefore their density increases in this region, see Fig. 1.
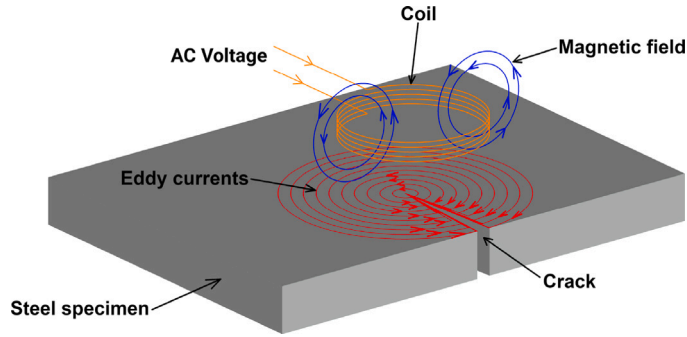

Fig. 1. Principle of the Eddy currents testing.

The density of the induced Eddy currents within the steel specimen is described by the skin effect, which causes that the density decays exponentially below the surface of the specimen, see [3,4]. The corresponding depth of penetration is known as skin depth, and it is given by

$$\delta = \sqrt{\frac{1}{\pi f \sigma \mu \mu_o}} \tag{1}$$

where

   f: frequency of the signal
   σ: electrical conductivity of the conductor
   μ: permeability of the conductor
   μ_o: permeability of the vacuum

Regions where Eddy currents density increases, experience a higher Joule heating, which can be observed with an IR camera, see [5,6]. The Joule heating is generated on the surface of the specimen and it is proportional to the square of Eddy currents density and to the diffused heat [7–9]. Thus, the Eddy current loss per unit volume is given by

$$\rho = \frac{\mu_0 (2\pi f)^2 W^2}{12\pi\sigma} \tag{2}$$

where

   μ_o: permeability of the vacuum
   f: frequency of the signal
   W: amplitude of the magnetic field
   σ: electrical conductivity of the material

Moreover, the Joule heating is immediately transferred into the inner part of the specimen by the thermal conductivity. The heat penetrates mainly into the depth determined by the thermal diffusion length, which can be calculated by

$$d_{th} = 2\sqrt{\kappa t} \tag{3}$$

where

   κ: thermal diffusivity of the conductor
   t: elapsed time

In case that the heat penetration d_{th} is larger that the penetration depth δ, the heat flux is determined by the thermal diffusivity of the material and not by the penetration depth of the induced Eddy currents [10,11].

In short, Eddy currents cause temperature increments at the surface of the specimen in the vicinity of the cracks. For this reason, this method can be applied only to detect surface cracks or discontinuities. In case that the material has an internal discontinuity, other methods have to be considered, see [12,13]

Most of the available applications focus on crack detection in the surface of small machine parts such as turbine blades, hydraulic system joints or metal plates, see [2,5,10,14–18]. In addition, the corresponding equipment requires a large amount of power, is large and heavy, so it cannot be used to inspect large steel structures on site.

Thus, in order to detect cracks caused by cyclic loading in large steel structures, we use a setup, which consumes less power and it is lighter than the setups used nowadays. A novel method to generate the high frequency AC voltage allows to reduce the power consumption and the weight of the necessary equipment.
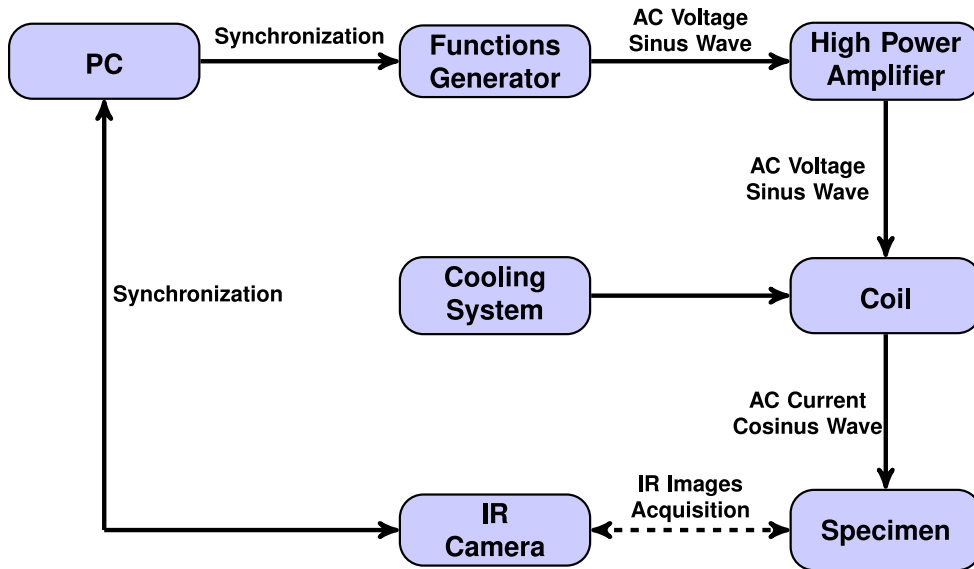
Fig. 2. Block diagram of the common crack detection setup.

The use of the proposed setup is performed as follows. In Section 2, the features and differences of the common setup and the proposed one are described. In Section 3, two specimens with induced fatigue cracks are tested. The first one is a steel plate with an internal notch and the second one is a welded tee joint. Finally, in Section 4, the conclusions and subsequent research are presented.

2. Common and alternative setup based on the Eddy currents principle

2.1. Common setup

The main differences between the common setup and the proposed one are the geometry of the AC voltage wave, the power consumption and the size of the involved equipment.

A common experimental setup to apply the Eddy currents principle consists of a high frequency functions generator, an amplifier, a coil, a cooling system, an IR camera and a PC, although in some cases two generators and two coils have been used [19,20], see Fig. 2.

The amount of required power to run a system with this configuration in some applications is from 2 kW up to 15 kW, see [10,21–24]. This fact represents the main limitation of this configuration to be applied as it is on real steel structures *in situ* such as bridges, beams, wind towers, offshore structures, rail tracks or heavy duty cranes. As a matter of fact, it has been applied mostly to test small specimens such as machinery parts and the corresponding equipment is very heavy and big to be portable. Even the current related standard [25] and the common non visual Eddy current detection [2] consider only this type of applications. Moreover, a subsequent image analysis is required, so that, the detection cannot be considered as performed in real time.

2.2. Alternative setup

The alternative setup used in this research recreates the Eddy currents principle by generating a square wave AC voltage from a DC voltage, which is supplied by a conventional power source. The square wave generation is performed by a control unit called S2S[1] Hi Speed Wave Induction Unit. The S2S unit allows to set the frequency, excitation time and off time of the square wave generation.

With this configuration, the functions generator and the high power amplifier are not required, so that, the power consumption and weight of the necessary equipment is considerably reduced [5].

Moreover, this setup offers the opportunity to detect the cracks on real time, so that, the time and cost of testing are also reduced. Fig. 3 shows the block diagram of the alternative crack detection setup.

The corresponding experimental setup is shown in Fig. 4.

Detailed information about the S2S unit is described in [26–28]. A review about some NDT techniques used for fatigue crack detection is presented in [29] and particularly in steel bridges is presented in [30], where the author also proposes a remote NDT technique using IR thermography for fatigue crack detection and structural integrity assessment of these structures.
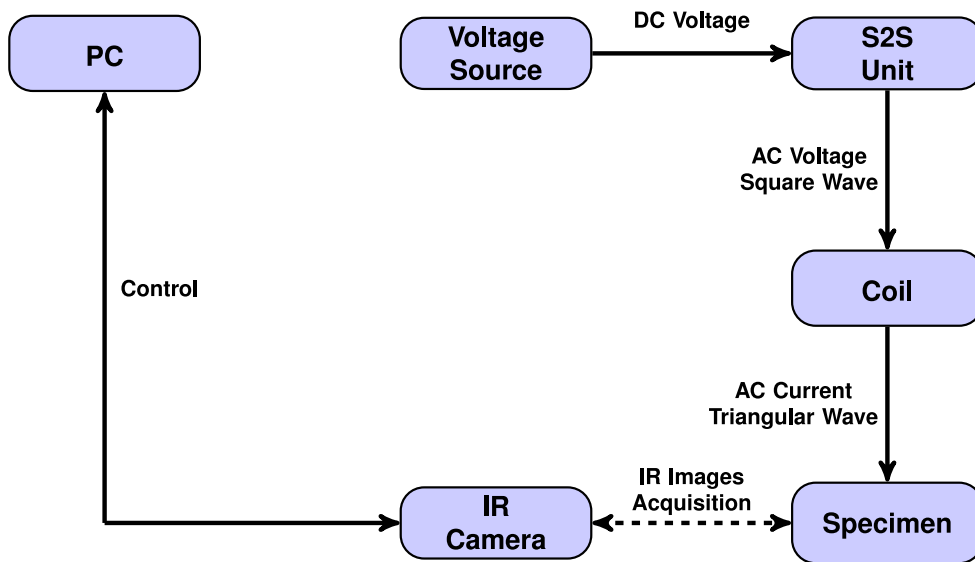
---

[1] S2S: Square to Shark.

Fig. 3. Block diagram of the alternative crack detection setup.

Fig. 4. Alternative crack detection setup. A: IR camera, B: coil, C: S2S unit, D: voltage supply, E: PC and F: steel specimen.
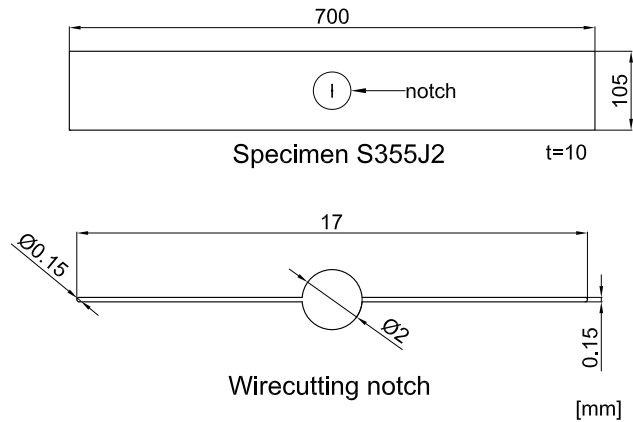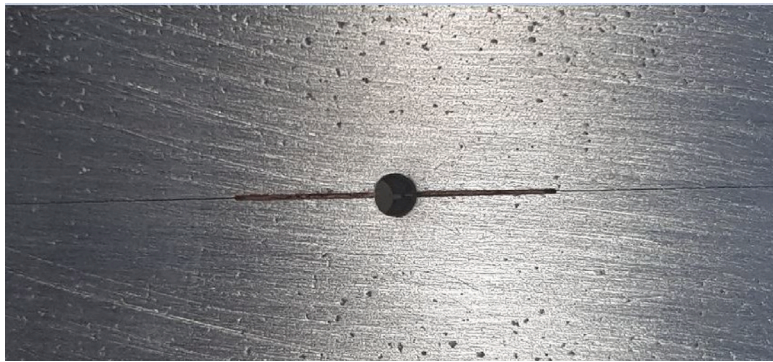
Fig. 5. Notched specimen made of steel S355J2.

Fig. 6. Crack growth at both sides of the notch while applying an axial tension force.

3. Application on notched and welded steel specimen

3.1. Notched specimen made of S355J2 steel

In this application a plate made of steel S355J2 is tested. In the middle of the plate a notch has been made by wire cutting. The geometry of the steel plate and the notch is shown in Fig. 5.

To induce crack growth at both sides of the notch up to 13 mm, the specimen was subjected to a cyclic loading of stress range $\Delta\sigma = 70$ MPa and stress ratio $R = 0.5$. The crack growth was monitoring by applying the electrical potential technique, see [31].

It is worth mentioning that the observed crack growths are not visible with a microscope. The only way to observe them was when the specimen was subjected to a tension force in order to avoid the internal clamping force on the notch, see Fig. 6. This fact makes very difficult to detect the crack growths by standards means of detection.

3.1.1. CAD and FEM simulation

In order to choice the optimal parameters to be applied during the experiments, a FEM simulation of the electromagnetic parameters caused by inducing an AC voltage into the coil was performed. This simulation was made by using the Maxwell 3D Design with solution type Eddy current from software ANSYS electronics. Nominal materials from the software, such as cast iron for the specimen, copper for the coil and vacuum for the environment were selected. The mesh properties also were defined by default in the software. The excitation time was 100 ms which is the same value used afterwards the experiments.

Moreover, comparing the simulation with the experimental results allows to see the effect of environmental conditions, which differ from the ideal conditions assumed in the simulation.

On Fig. 7 the steel specimen and the position of the coil for the simulation are displayed.

The results of the simulation can be observed in Fig. 8. Fig. 8(a) shows the grid of the steel specimen, Fig. 8(b) shows the Ohmic loss, which causes the temperature variation. Fig. 8(c) displays the current density in the surface of the plate and Fig. 8(d) shows the temperature reached on the surface of the steel specimen during the square wave excitation. In Figs. 8(b) to 8(d), the corresponding parameters reach their high value at the crack tip. Among of them, the most relevant one is the temperature, since its variation will be observed and recorded with the IR camera. This fact represents the ideal effect that is expected to reach with the experiments.

(a) Global view of the specimen and the coil

(b) Detailed view

(c) CAD Global view of the specimen and the coil

(d) Detailed view
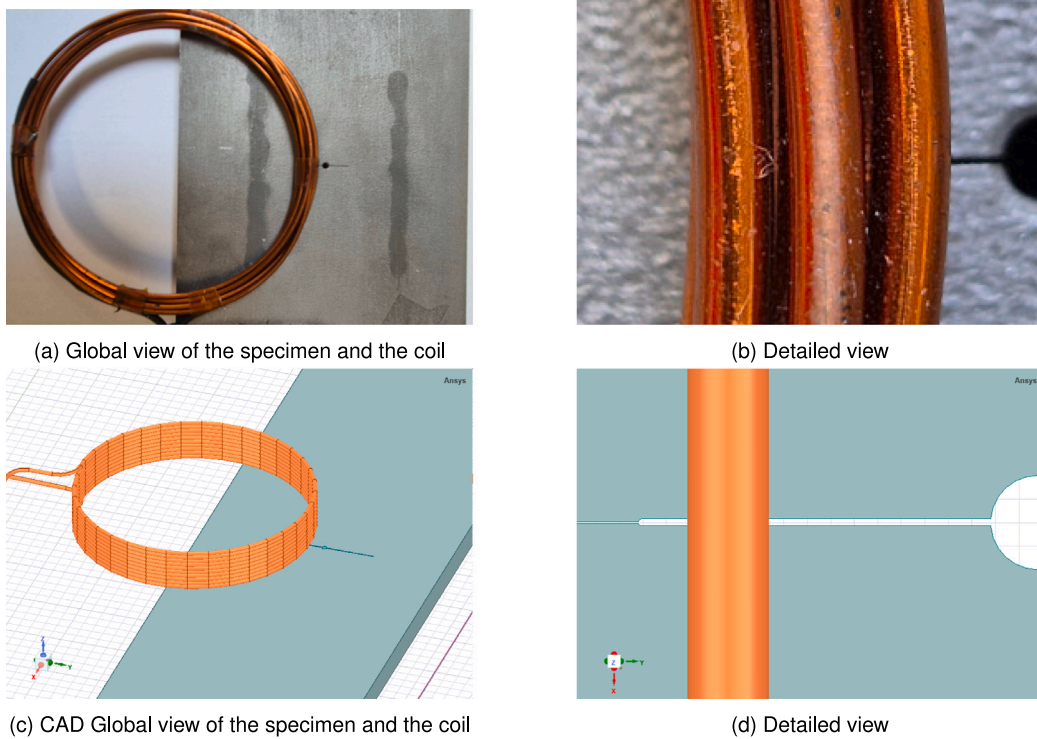
Fig. 7. Specimen and coil position considered in the experiment and FEM simulation.

(a) Grid

(b) Ohmic Loss

(c) Current density

(d) Temperature

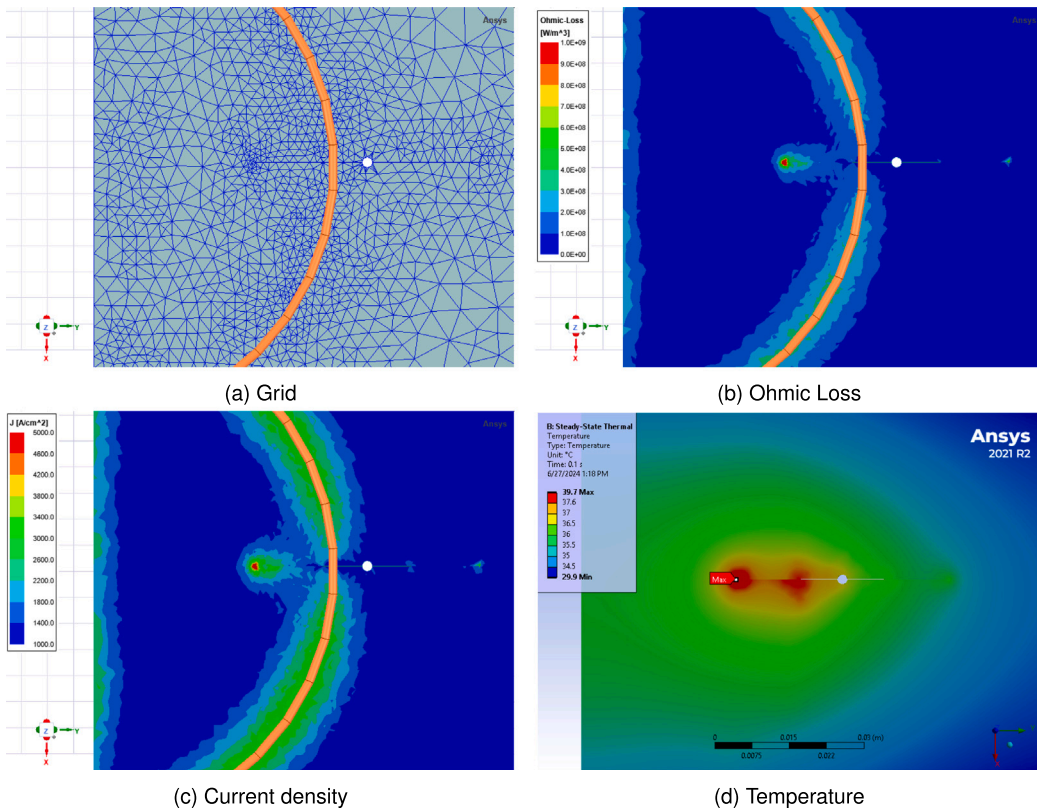**Fig. 8.** FEM Simulation results.
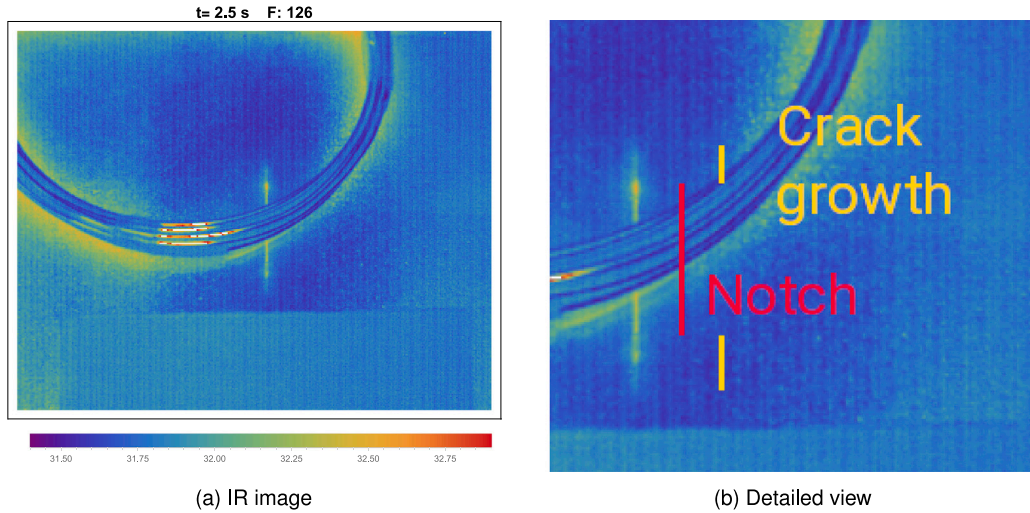
(a) IR image   (b) Detailed view

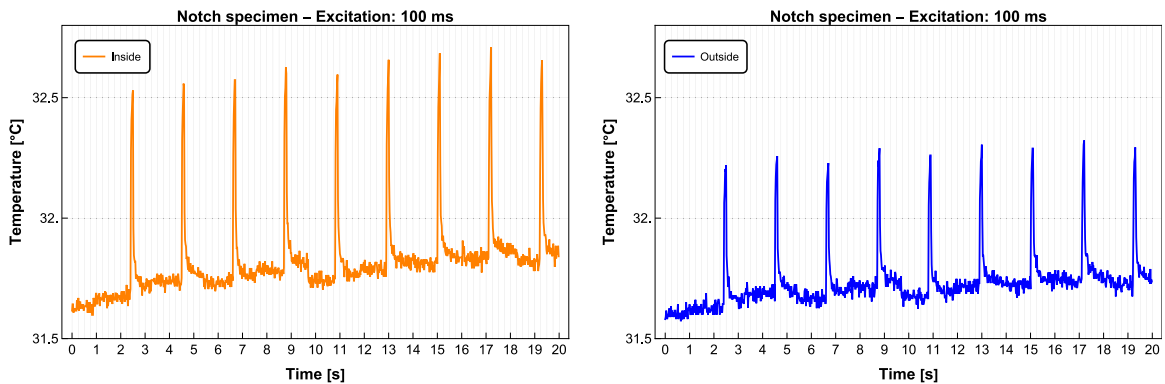**Fig. 9.** Detection of the crack while the coil is located in the middle of the notch.

Fig. 10. Temperature evolution at the crack tip during the experiment.

3.1.2. Experiments

The first experiments were performed by locating the coil right over the middle of the notch in order to see how the temperature increases on both sides of the crack. The parameters of the experiments are described in Table 1.

The Fig. 9(a) shows the IR image when the maximum temperature is reached.

In these experiments not only the notched was visible but the crack growth as well, see Fig. 9(b). As it was mentioned, the crack growth was not visible with a microscope, so that, this fact represents an important asset in the application of the alternative crack detection system.

As expected and according to the simulation, the crack tips and the notch vertices at both sides reach their highest temperature during the electromagnetic excitation. As a matter of fact, the crack tip located in the interior area of the coil reaches a higher temperature than the crack tip located in the exterior area of the coil, see Fig. 10.

In order to analyze the effect of moving the coil closer to the crack tip and of the square wave frequency, a second series of experiments were performed, see Table 2.

Four locations of the coil were considered. A: Center of the notch, B: Between center and notch vertex, C: Close to the notch vertex and D: Between crack tip and notch vertex, see Fig. 11. The corresponding IR images are shown on Fig. 12.

Similar to the first experiments, the notch vertices and the crack tips at both sides of the notch were detected when the coil was located in the center of the notch. Moreover, as expected a higher temperature is reached inside the coil, see Fig. 12(a). A better visualization of the crack vertex and crack tip inside the coil is obtained when the coil is located among the center and the vertex of the notch, see Fig. 12(b). This image is similar to Fig. 8(d) from the simulation. By moving the coil close to the internal vertex, the internal crack tip and the internal crack geometry is observed, see Fig. 12(c). Finally, when the coil is located between the crack tip and the notch vertex, only the first one is observed, see Fig. 12(d).

Table 1

Experimental parameters while the coil is located in the middle of the notch.

Parameter	Value	Unit
DC voltage	120	V
Square wave frequency	120	kHz
Excitation time	100	ms
Off time	2	s
Recording time	20	s
Recording frequency	50	Hz

Table 2

Experimental parameters by different coil locations.

Parameter	Value	Unit
DC voltage	110	V
Square wave frequency	90–120	kHz
Excitation time	200	ms
Off time	3	s
Recording time	10	s
Recording frequency	200	Hz

Table 3

Maximum temperature reached in different regions of the crack depending on the position of the coil. A: Center of the notch, B: Between center and notch vertex, C: Close to the notch vertex and D: Between crack tip and notch vertex.

Region of interest	Coil position			
	A	B	C	D
Tip inside	33.30	34.02	32.90	33.57
Vertex inside	32.87	33.37	33.79	32.94
Tip outside	32.82	32.44	32.45	32.47
Vertex outside	32.79	32.45	32.41	32.43

The corresponding temperature variation at the notch vertices and crack tips are displayed in Fig. 13. The maximum temperature reached in these regions of the crack depending on the position of the coil are shown in Table 3. On the one hand, the internal vertex reaches the highest temperature when the coil is position B, see Fig. 13(b) and the internal crack tip when the coil is in position C. On the other hand, the external notch vertex and crack tip reach the lowest temperature when the coil is furthest from the notch center, see Fig. 13(d). The behavior of the temperature variation as function of the coil position is related with the Ohmic loss caused by the electromagnetic field which is generated inside and outside of the coil. On the one hand, the electromagnetic field is stronger inside the coil than outside. On the other hand, it is weaker in the center of the coil. Moreover, since the heat flux depends on the elapsed time as shows Eq. (3), the higher temperature are reached in the crack regions close to the coil because of the thermal conductivity.

It is worth mentioning that if temperature variation is very low, an IR camera with a higher sensitivity is required. A similar situation is also mentioned in [19].

Finally, in order to see the effects of the excitation frequency on the temperature variation of the internal notch vertex and crack tip, coil locations B and C are considered.

In location B, the temperature increases as the excitation frequency is reduced. The major change is observed from 115 kHz to 110 kHz, see Fig. 14(a). In location C, the effect of the excitation frequency on the temperature variation is negligible, see Fig. 14(b). The effect of the frequency is related to the skin effect give by Eq. (1). The greater the skin depth into the material, the greater the region through which the heat flows.

Based on these results, an excitation of 110 kHz seems to be suitable to perform a reliable detection. Similar results are obtained in [19,32]. The corresponding results are shown in Table 4.

3.2. Welded specimen made of SM490 steel

In this application a tee joint with a convex fillet weld made of SM490[2] steel has been tested. The specimen and the location of the coil are shown in Fig. 15.

An eccentric motor was attached to the steel specimen as shown in Fig. 16. By rotating the eccentric motor, resonant vibrations are generated, and a repeated bending load is applied to the specimen. The stress ratio was adjusted by setting the spring on the left in the picture.

---

[2] This is a Japanese steel, whose grade is equivalent to S355J2 European steel.

(a) A: center of the notch

(b) B: between center and notch vertex

(c) C: close to the notch vertex

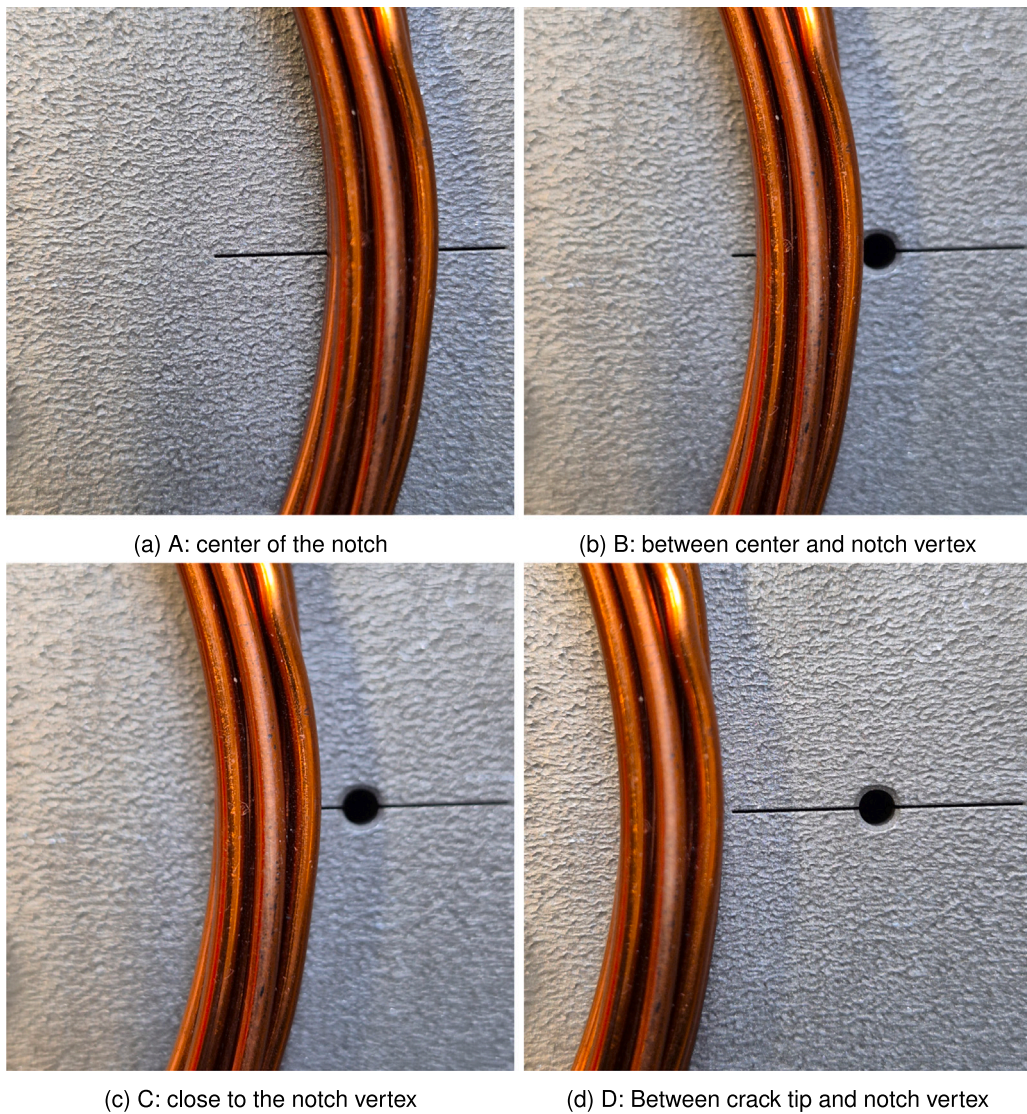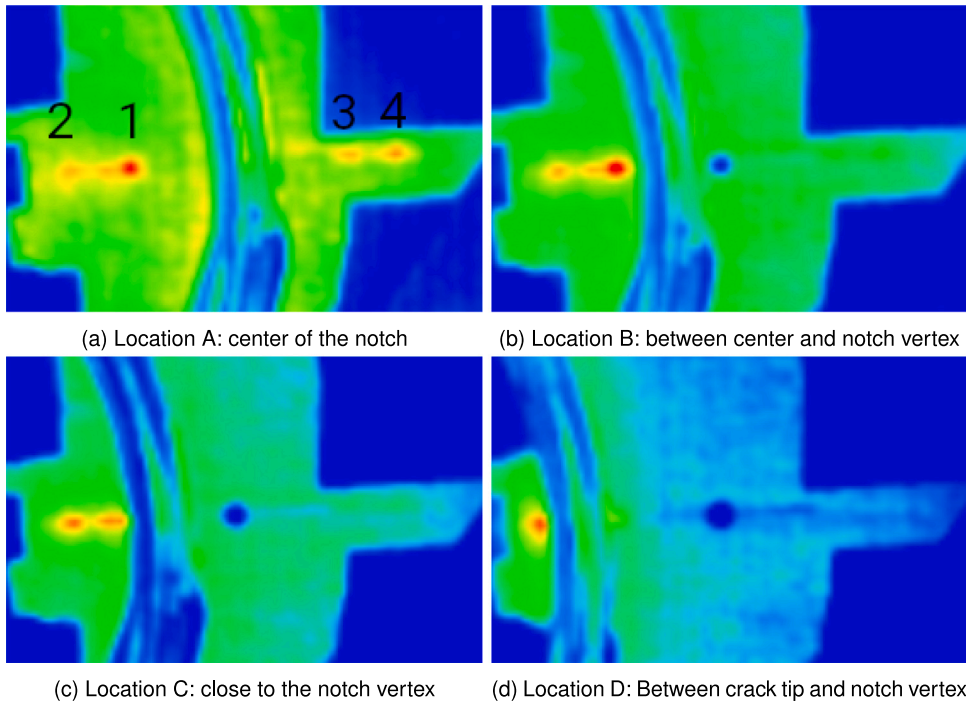(d) D: Between crack tip and notch vertex

Fig. 11. Coil locations considered to study their influence on the temperature variation on the crack edges.

Table 4
Temperature variation reached in the internal crack vertex and tip depending on the excitation frequency and positions B and C of the coil. B: Between center and notch vertex, C: Close to the notch vertex.

Frequency	B		C	
[kHz]	Vertex	Tip	Vertex	Tip
90	1.78	1.27	2.53	1.78
95	1.66	1.15	2.57	1.84
100	1.62	1.22	2.41	1.67
105	1.60	1.06	2.27	1.51
110	1.51	0.84	2.20	1.40
115	0.77	0.58	2.26	1.30
120	0.72	0.71	2.27	1.31

The applied stress was calculated by applying strain gauges. The strain gauges were attached to a location that was not affected by stress concentration due to the weld toe. The loading frequency was set to 18.1 Hz, the maximum applied stress to 80 MPa and the stress ratio to $R = 0$.

(a) Location A: center of the notch

(b) Location B: between center and notch vertex

(c) Location C: close to the notch vertex

(d) Location D: Between crack tip and notch vertex

Fig. 12. IR images by considering different coil locations A, B, C,D. Reference points 1: Notch vertex inside the coil, 2: Crack tip inside the coil, 3: Notch vertex outside the coil and 4: Crack tip outside the coil.

Table 5
Experimental parameters applied on the welded specimen.

Parameter	Value	Unit
DC voltage	120	V
Square wave frequency	120	kHz
Excitation time	100	ms
Off time	3	s
Recording time	12	s
Recording frequency	50	Hz

The applied cyclic loading induced cracks at both sides of the welding toe, see Fig. 17. The length of the left crack is 18,44 mm and of the right crack is 10,44 mm.

3.2.1. CAD and FEM simulation

As in the previous application, a FEM simulation of the electromagnetic field with the same properties was performed with ANSYS electronics. The CAD model of the welded specimen and the coil is shown in Fig. 18(a) and the crack geometry is displayed in Fig. 18(b).

The results of the simulation can be observed in Fig. 19. Particularly, Fig. 19(a) shows the grid of the steel specimen, Fig. 19(b) shows the Ohmic loss, which causes the temperature variation. Fig. 19(c) displays the current density in the surface of the specimen and Fig. 19(d) shows the temperature on the surface of the specimen, which was caused by the square wave excitation. As it is observed in Figs. 19(b) to 19(d), the corresponding parameters reach their high value at the crack tip as well.

3.2.2. Experiments

The experiments were performed by locating the coil close to the vertical plate and the welding toe. In this paper the results corresponding to the left crack are presented. Since the results from the right side are very similar, they are not included.

The parameters of the experiments are described in Table 5.

Fig. 20 shows the obtained IR images corresponding to crack detection on the left side. These images depict the instants when the maximum temperature was reached at the crack tip.

As expected and according to the simulation, the crack tip reaches its highest temperature during the square wave excitation. This fact occurs at time $t = 2.7, 5.8, 8.9, 12$ s.
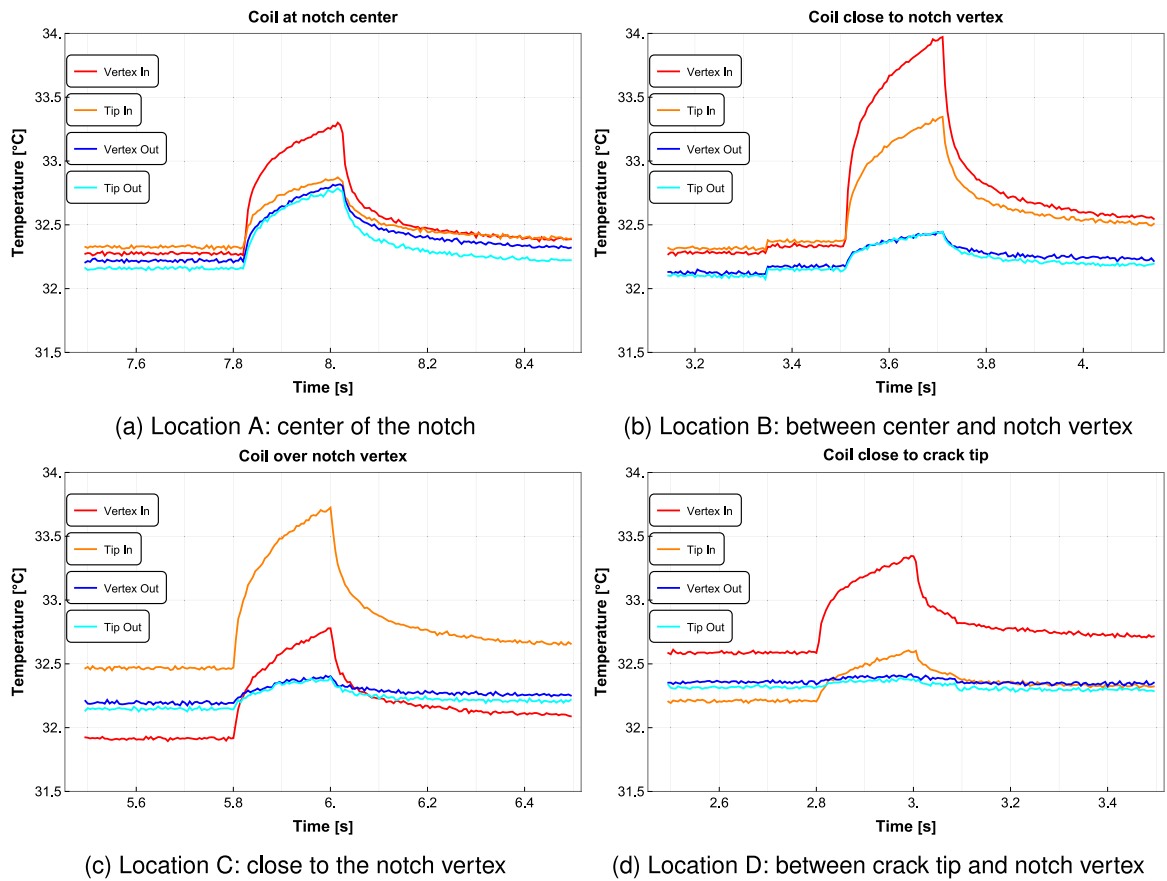
Fig. 13. Temperature variation by considering different coil locations. Applied excitation frequency 100 kHz.
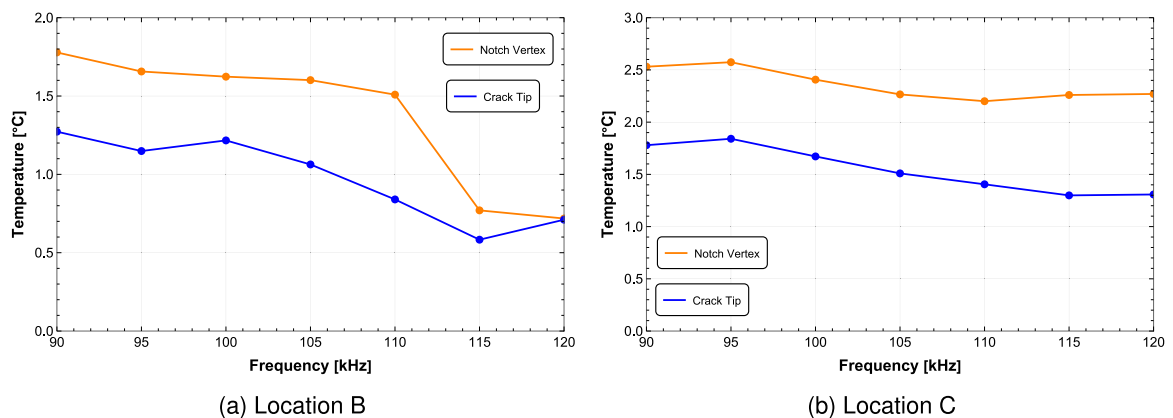

Fig. 14. Temperature variation at the notch vertex and crack tip depending on the square wave frequency.

The temperature evolution at the crack tip during the complete experiment is depicted in Fig. 21(a). The four peaks observed during the excitation are those corresponding to the maximum reached temperature. The Fig. 21(b) shows in detail the increment of the temperature during the 100 ms of the second excitation. As expected, the heating and cooling of the crack tip show the typical shark wave geometry.

(a) Global view of the specimen and the coil   (b) Detailed view

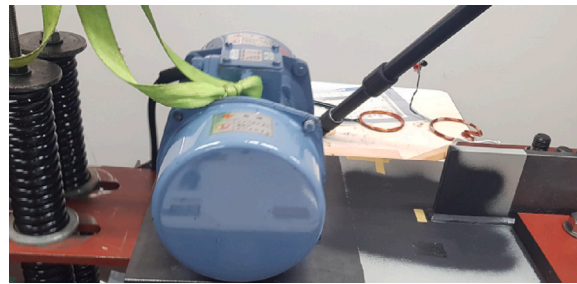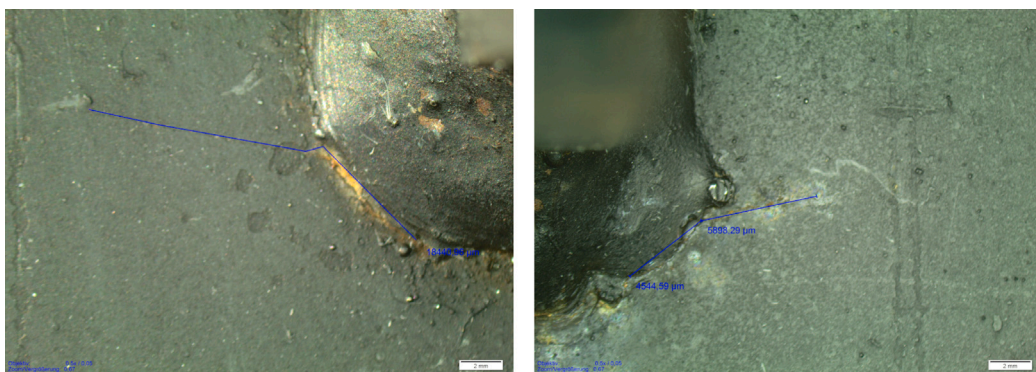**Fig. 15.** Welded tee joint made of SM490.

Fig. 16. Cyclic loading setup.

(a) Left side   (b) Right side

Fig. 17. Cracks induced by the fatigue experiment.

It is worth mentioning that the temperature variation caused by the square wave excitation shows different geometries depending on the considered region on the specimen. Thus, at the crack tip it shows the typical shark wave geometry, while on other regions, such as the coil, the steel plate inside or outside the coil, it behaves differently, see Fig. 22.
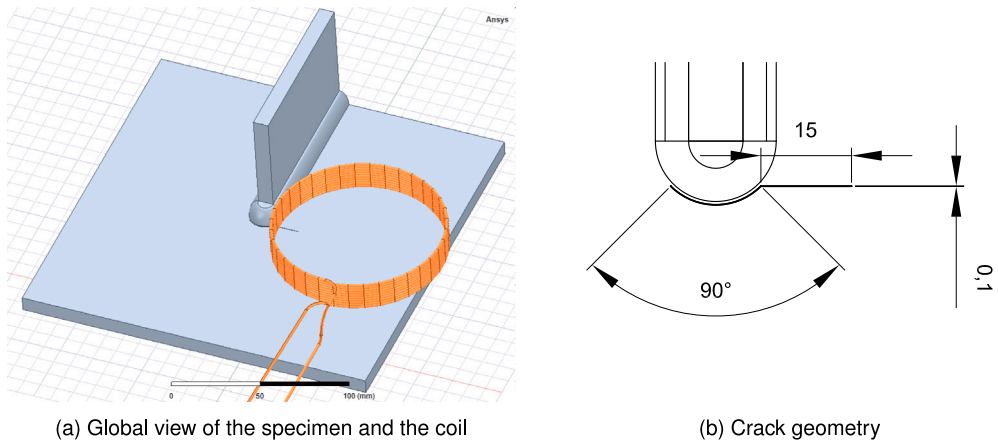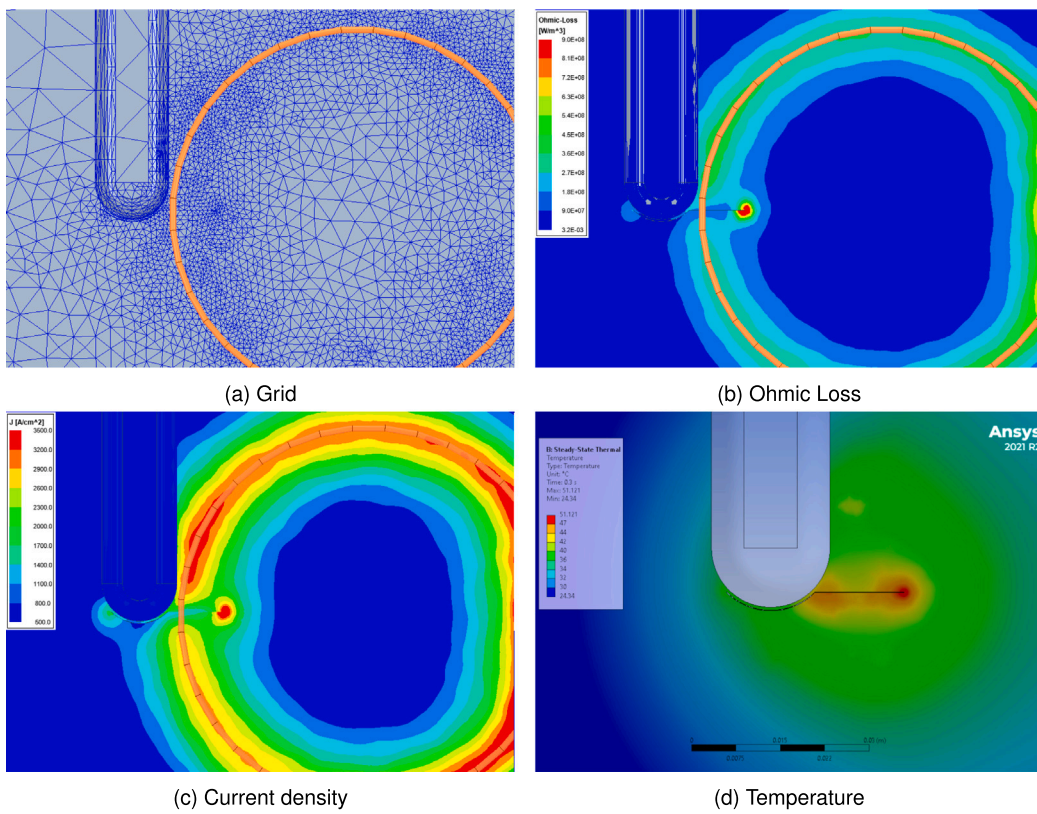
(a) Global view of the specimen and the coil

(b) Crack geometry

Fig. 18. CAD model of the welded specimen.

(a) Grid

(b) Ohmic Loss

(c) Current density

(d) Temperature

Fig. 19. FEM Simulation results.

t= 2.7 s   F: 134

t= 5.8 s   F: 289

t= 8.9 s   F: 444

t= 12.0 s   F: 599
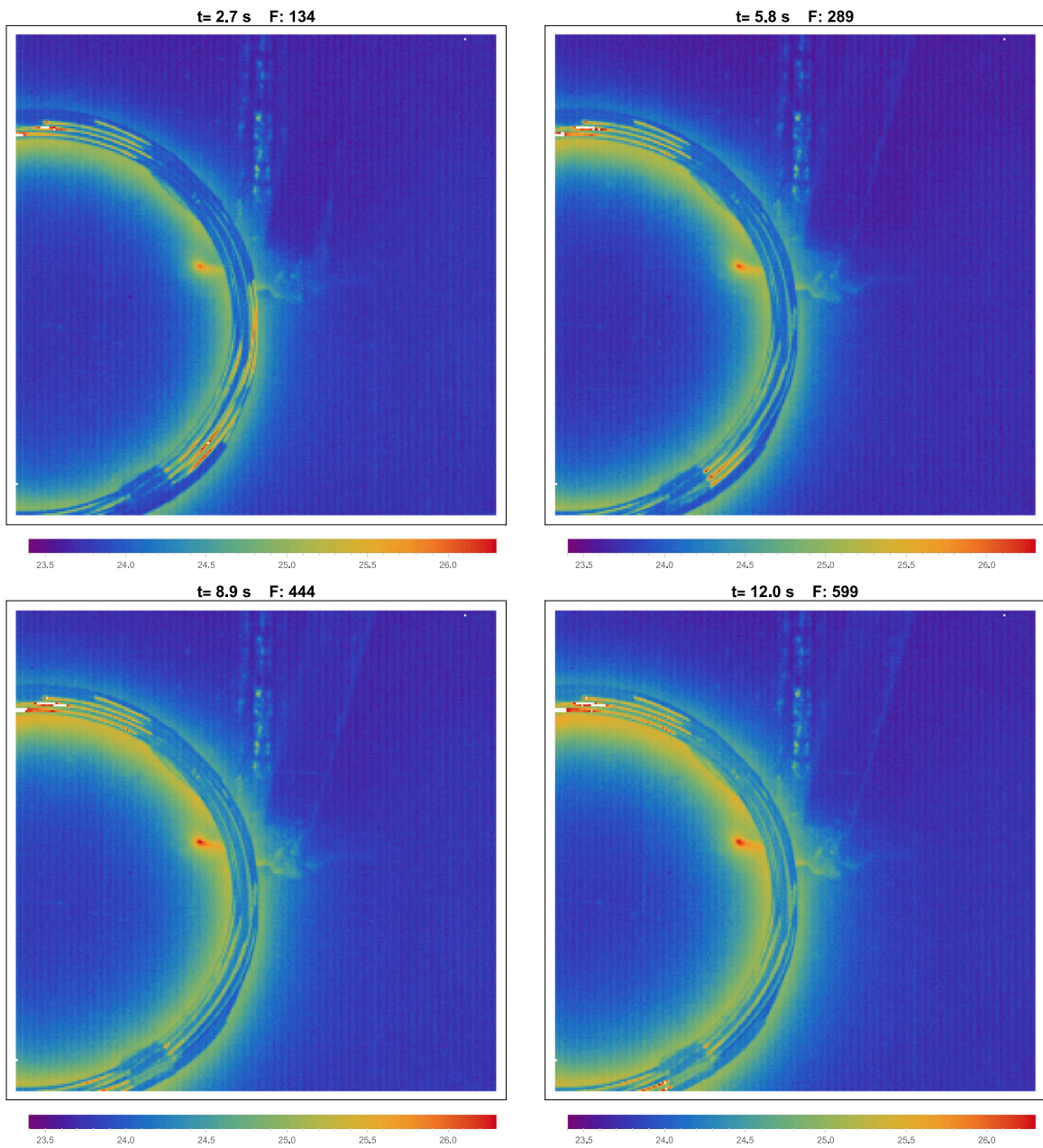
Fig. 20. Detection of the left crack. Infrared images when the square wave excitation is activated.

(a) Complete experiment

(b) Shark wave geometry of the second excitation

Fig. 21. Temperature evolution at the crack tip during the experiment.

(a) Selected points
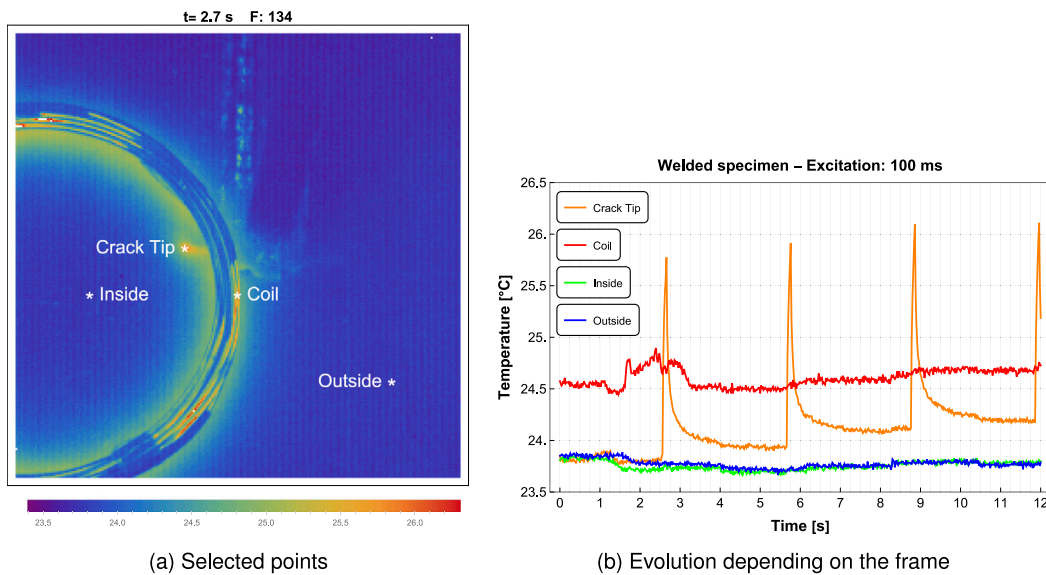
(b) Evolution depending on the frame
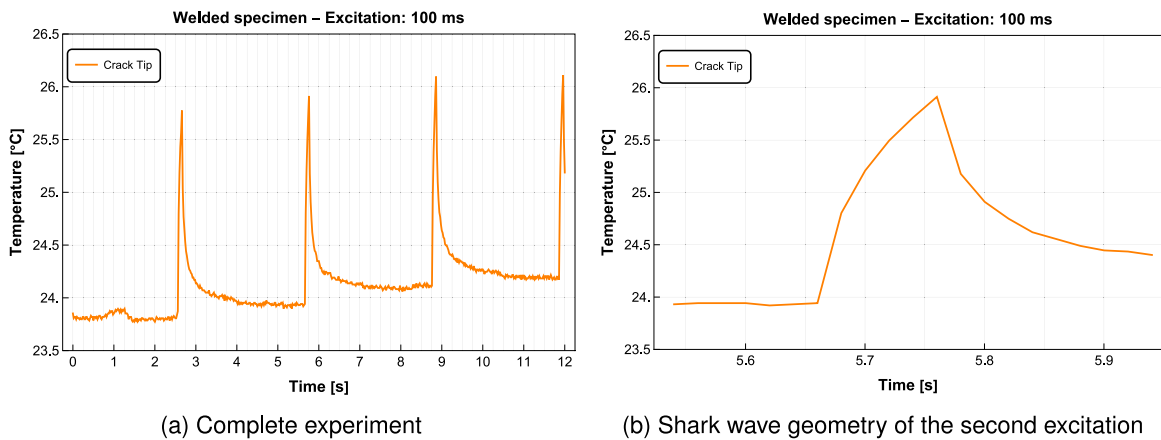
Fig. 22. Comparison of the temperature evolution in different regions during the experiment.

4. Conclusions and subsequent research

As it has been observed in both applications, the crack detection and observation were clear and immediate. In other words, the crack detection can be considered as performed in real time.

The coil position and the square wave frequency play a relevant role in the detection. On the one hand, the biggest temperature variation is obtained when the crack tip is inside and close to the coil. On the other hand, the most appropriate frequency is between 100 kHz and 110 kHz.

The experimental setup used in this research has proven to be suitable for detecting cracks on the surface of steel structures under laboratory conditions. It also requires much less energy than common systems. Since the system is portable and lightweight, it is suitable for inspecting and monitoring large steel structures on site. This represents a great potential in the monitoring of crack initiation and propagation on bridges, offshore oil installations, railroad rails, wind energy towers, and other structures. The corresponding costs can thus be reduced considerably.

Despite the promising results obtained during this research, there are still some aspects, which deserve attention. On the one hand, from the power electronics point of view, the device will be completely portable if the necessary voltage is supplied by rechargeable batteries. Moreover, taken into account that there exist different details in steel structures, a new geometry of the coil has to be designed and studied for every need. On the other hand, regarding the applications, the influence of the coating by performing the crack detection is a topic to be investigated.

Finally, performing detection experiments on large steel structures *in situ* will help to evaluate the reliability of the system under normal environmental conditions.

CRediT authorship contribution statement

Paul Dario Toasa Caiza: Writing – original draft, Funding acquisition, Conceptualization. **Daiki Shiozawa:** Writing – review & editing, Validation, Methodology, Investigation. **Thomas Ummenhofer:** Validation. **Takahide Sakagami:** Validation, Investigation.

Declaration of competing interest

The authors declare no potential conflict of interests.

Data availability

Data will be made available on request.

Acknowledgments

References

[1] X. Maldague, Theory and Practice of Infrared Technology for Nondestructive Testing, John Wiley & Sons, Inc., 2001.

[2] Z.L. Amanda To, S. Dixon, Improved detection of surface defects at sample edges using high-frequency eddy current amplitude and phase measurements, Nondestruct. Test. Eval. 37 (6) (2022) 795–819, http://dx.doi.org/10.1080/10589759.2022.2063858.

[3] W.H. Hayt, J.A. Buck, Engineering Electromagnetics, ninth ed., McGraw-Hill Higher Education, 2018.

[4] B. Oswald-Tranta, Thermoinductive investigations of magnetic materials for surface cracks, Quant. InfraRed Thermogr. J. 1 (1) (2004) 33–46, http://dx.doi.org/10.3166/qirt.1.33-46.

[5] U. Netzelmann, Induction thermography of surface defects, in: Handbook of Advanced Nondestructive Evaluation, Springer International Publishing, Cham, 2019, pp. 1497–1522, http://dx.doi.org/10.1007/978-3-319-26553-7_31.

[6] Y.-K. Zhu, G.-Y. Tian, R.-S. Lu, H. Zhang, A review of optical NDT technologies, Sensors 11 (8) (2011) 7773, http://dx.doi.org/10.3390/s110807773.

[7] N.J. Siakavellas, The influence of the heating rate and thermal energy on crack detection by eddy current thermography, J. Nondestruct. Eval. 35 (2) (2016) 29, http://dx.doi.org/10.1007/s10921-016-0337-9.

[8] W. Hurley, W. Wölfle, Transformers and Inductors for Power Electronics, John Wiley & Sons Ltd, 2013.

[9] J. Wilson, G. Tian, I. Mukriz, D. Almond, PEC thermography for imaging multiple cracks from rolling contact fatigue, NDT&E Int. 44 (6) (2011) 505–512, http://dx.doi.org/10.1016/j.ndteint.2011.05.004.

[10] B. Oswald-Tranta, Induction thermography for surface crack detection and depth determination, Appl. Sci. 8 (257) (2018) http://dx.doi.org/10.3390/app8020257.

[11] B. Oswald-Tranta, Thermo-inductive crack detection, Nondestruct. Test. Eval. 22 (2–3) (2007) 137–153, http://dx.doi.org/10.1080/10589750701448225.

[12] D. Wu, L. Yin, Y. Gao, Z. Miao, Y. Wang, Internal crack detection based on thermal excitation enabled digital image correlation method, Measurement 227 (2024) 114262, http://dx.doi.org/10.1016/j.measurement.2024.114262.

[13] N. Ranc, A. Messager, A. Junet, T. Palin-Luc, J. Buffière, N. Saintier, M. Elmay, L. Mancini, A. King, Y. Nadot, Internal fatigue crack monitoring during ultrasonic fatigue test using temperature measurements and tomography, Mech. Mater. 174 (2022) 104471, http://dx.doi.org/10.1016/j.mechmat.2022.104471.

[14] B. Oswald-Tranta, Detection and characterisation of short fatigue cracks by inductive thermography, Quant. InfraRed Thermogr. J. 19 (4) (2022) 239–260, http://dx.doi.org/10.1080/17686733.2021.1953226.

[15] R.A.V. Hidalgo-Gato, E. Gorostegui-Colinas, P.L. de Uralde, A. Muniategui, B. Urtasun, I. Silanes, Automated defect detection based on time and frequency domain analysis using Eddy Current Pulsed Thermography in EB and TIG welding inspections, in: Proceedings of the 2020 International Conference on Quantitative InfraRed Thermography, 2020.

[16] J. Vrana, M. Goldammer, Induction and conduction thermography: From the basics to application, in: Thermographie-Kolloquium 2017, DGZfP, 2017.

[17] M. Goldammer, H. Mooshofer, M. Rothenfusser, J. Bass, J. Vrana, Automated induction thermography of generator components, AIP Conf. Proc. 1211 (1) (2010) 451–457, http://dx.doi.org/10.1063/1.3362428.

[18] W. Hassan, C. Homma, Z. Wen, F. Vensel, B. Hogan, Detection of tight fatigue cracks at the root of dampers in fan blades using sonic IR inspection: A feasibility demonstration, AIP Conf. Proc. 894 (1) (2007) 455–462, http://dx.doi.org/10.1063/1.2718007.

[19] X.-T. Xiao, Z. Liang, L. Zhang, S. Tang, Design and investigation of a two-coil magnetic core inductor used for Eddy current pulsed thermography, Measurement 174 (2021) 109063, http://dx.doi.org/10.1016/j.measurement.2021.109063.

[20] B. Oswald-Tranta, M. Sorger, Localizing surface cracks with inductive thermographical inspection: from measurement to image processing, Quant. InfraRed Thermogr. J. 8 (2) (2011) 149–164, http://dx.doi.org/10.3166/qirt.8.149-164.

[21] Y. Liu, G. Tian, B. Gao, X. Lu, H. Li, X. Chen, Y. Zhang, L. Xiong, Depth quantification of rolling contact fatigue crack using skewness of eddy current pulsed thermography in stationary and scanning modes, NDT&E Int. 128 (2022) 102630, http://dx.doi.org/10.1016/j.ndteint.2022.102630.

[22] C. Tuschl, B. Oswald-Tranta, D. Künstner, Schienenprüfung Mittels Induktiv Angeregter Thermografie, DACH Jahrestagung, 2019.

[23] Y. Wang, X. Gao, U. Netzelmann, Detection of surface cracks in metals under coatings by induction thermography, in: 14th Quantitative InfraRed Thermography Conference, 2018.

[24] U. Netzelmann, G. Walle, S. Lugin, A. Ehlen, S. Bessert, B. Valeske, Induction thermography: principle, applications and first steps towards standardisation, Quant. InfraRed Thermogr. J. 13 (2) (2016) 170–181, http://dx.doi.org/10.1080/17686733.2016.1145842.

---

[3] Deutsche Forschungsgemeinschaft.

[25] DIN 54183:2018-02 Non-Destructive Testing - Thermographic Testing - Eddy-Current Excited Thermography, Standard, DIN Deutsches Institut für Normung e.V., Berlin, Germany, 2018.

[26] P.D. Toasa Caiza, R. Schwendemann, P. Calero, T. Ummenhofer, Portable generator to detect cracks on large steel structures: An application of inductive thermography, J. Nondestruct. Eval. 40 (63) (2021) 1–11, http://dx.doi.org/10.1007/s10921-021-00795-5.

[27] R. Schwendemann, M. Lorcher, F. Sommer, L. Stefanski, M. Hiller, A new, universal series hybrid cascaded H-bridge converter for power-hardware in the loop emulation, in: 2019 21st European Conference on Power Electronics and Applications, EPE '19 ECCE Europe, 2019, pp. P.1–P.10, http://dx.doi.org/10.23919/EPE.2019.8914925.

[28] I. Trausch, Entwurf und Inbetriebnahme einer MOSFET H-Brückenschaltung für eine Zerstörungsfreie Werkstoffprüfung (B.Sc. Thesis), Intitute of Electrical Engineering (ETI). Karlsruhe Institute of Technology (KIT), 2019.

[29] Z. Qu, P. Jiang, W. Zhang, Development and application of infrared thermography non-destructive testing techniques, Sensors 20 (14) (2020) 3851, http://dx.doi.org/10.3390/s20143851.

[30] T. Sakagami, Remote nondestructive evaluation technique using infrared thermography for fatigue cracks in steel bridges, Fatigue Fract. Eng. Mater. Struct. 38 (7) (2015) 755–779, http://dx.doi.org/10.1111/ffe.12302.

[31] G. Aronson, O. Ritchie, Optimization of the electrical potential technique for crack growth monitoring in compact test pieces using finite element analysis, J. Test. Eval. JTEVA 7 (4) (1979) 208–215.

[32] D. De Vanna, E. D'Accardi, G. Dell'Avvocato, D. Palumbo, U. Galietti, Induction thermography: Influence of testing parameters for different crack geometry, in: C. Franck, K. Kasza, J. Estrada, R. De Finis, G. Ólafsson, S. Gururaja, J. Furmanski, A. Forster, P. Kolluru, M. Prime, T. Berfield, C. Aydiner (Eds.), Challenges in Mechanics of Biological Systems and Materials, Thermomechanics and Infrared Imaging, Time Dependent Materials and Residual Stress, Volume 2, Springer Nature Switzerland, Cham, 2024, pp. 73–82.